Cramér–Rao Bound Evaluations of Compton Imager Designs for Proton Beam Range Verification

Daniel Shy, Jeffrey A. Fessler, *Fellow, IEEE*, Jerimy C. Polf, and Zhong He, *Senior Member, IEEE*

Abstract—Compton imaging is an attractive tool for range verification and dose estimation in proton therapy. To investigate the application of CdZnTe-based cameras for this task, we apply the uniform Cramér–Rao bound (UCRB) to dual-plane-based designs with various interplane spacings and evaluate their bias-variance tradeoff. The investigation focuses on the 718-keV and 4.4-MeV prompt gammas emitted from proton interactions with ^{12}C, and focuses on a detector geometry having two planes of 3×3 CdZnTe crystals with a volume of $2 \times 2 \times 1.5$ cm^3. When considering only interplane events, the improvement in minimum variance plateaus at 8 cm. However, when considering both intraplane and interplane events with an efficiency factor, the optimum spacing is calculated to be around 4 cm as larger spacings degrade the performance with poorer efficiency and a lower interplane to intraplane fraction. In addition, the study uses the modified UCRB based on a simulated distribution of prompt gamma rays expected from proton irradiation. The results show that the optimum spacing may be between 2 and 4 cm, depending on the specific bias-gradient norm.

Index Terms—Beam range verification, bias-variance tradeoff, compton imager design, compton imaging, Cramér–Rao lower bound (CRLB), proton therapy.

I. INTRODUCTION

HADRON therapies, or specifically proton therapy, are increasing in popularity with a rising number of available clinics worldwide to treat cancer [1]. Its attractiveness relies on the physical proton-matter interactions that result in the dose's maximum that is constrained to a localized region, also known as the Bragg peak [2], [3]. Therefore, therapies can be designed to deliver very conformal beams with the potential of delivering a high dose to a targeted area while minimizing unwanted dose to healthy tissue [4].

A challenge remains to verify the beam range and quantify the deposited dose during treatment [5], [6]. Several *in-vivo* methods are currently under investigation or clinically practiced, including positron emission tomography [7] and prompt gamma rays for spectroscopic [8], timing [9], prompt gamma peak integration [10], or imaging [11]–[14]-based techniques.

Compton imaging is an alternative to slit-based cameras as it eliminates the collimation system giving it the potential for superior detection efficiency [15]. Several prototypes have been developed using either scintillators, semiconductor-based detectors, or a combination of the two [12], [16]–[18].

This work investigates the design of CdZnTe-based Compton imagers for the application of proton beam range verification. Specifically, we report a bias-variance study that characterizes the distance between arrays of CdZnTe detectors (interplane distance). One of the more common methods of imager design is to grade its performance against a phantom and some known source distribution. For example, Monte Carlo simulation can quantify the possible image resolution performance of the system [19], [20]. Such simulations can also quantify the effects of detector size and spacing on the efficiency of the system [21], [22]. Furthermore, various experiments can optimize the design by studying the image response of the system when altering it [23].

Our approach uses the uniform Cramér–Rao bound (UCRB) as a tool for imager design and optimization [24]. The method's advantage is that it evaluates the systems independently of the estimator's characteristics. Studies that compare different systems based on their image response with unoptimized estimators may result in invalid conclusions [25]. The UCRB has been previously applied in Compton cameras [26] and compared against mechanically collimated systems [25], [27]. The unbiased Cramér–Rao bound was proposed for detector design in proton range estimation with spatial, spectral, and temporal criteria [28]. This work analyzes the Compton camera design for the application in beam range verification using the uniform and modified Cramér–Rao bound.

We consider an 18 crystal system with each crystal having the dimension of $2 \times 2 \times 1.5$ cm^3. The crystals are arranged into two planes of 3×3 individual crystals. Fig. 1 presents a diagram of the simulated system with the interplane distance labeled. The analysis focuses on two gamma-ray energies: 1) the 718-keV and 2) 4.4-MeV photons from the inelastic interactions of the proton on ^{12}C [29]. The analysis covers both the response to a point source with both energies and a 4.4-MeV prompt gamma-ray distribution from a simulated proton beam.
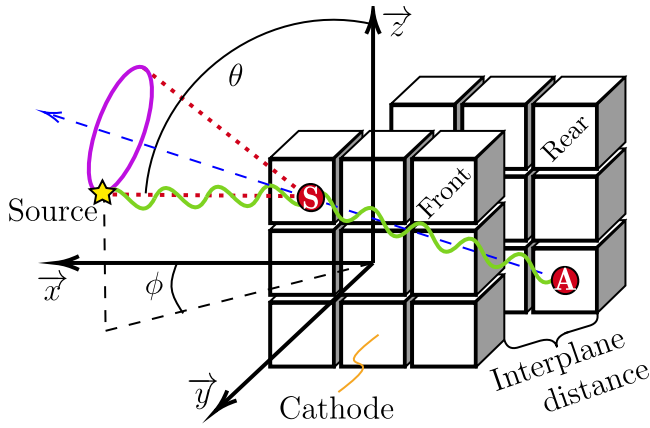
Fig. 1. Diagram of the 18 crystal system arranged in two arrays of 3×3 crystals. For both the front and rear plane, the normal of the cathode is pointed toward the y-direction. Also depicted is a Compton cone/ring, colored in red and purple, respectively. The green squiggly line represents the gamma ray's trajectory that is emitted from a source (yellow star). Depicted is a gamma ray that has scattered in a location marked by an "S" red dot and absorbed in the "A" red dot. The interplane distance is labeled and describes the distance between the anode of the front plane and the cathode of the rear plane.

The remainder of this article is organized as follows. Section II provides a mathematical introduction to the Cramér–Rao lower bound (CRLB) analysis. It then expands on to the UCRB followed by the modified UCRB (M-UCRB). Section III outlines the simulation methods applied in the system's modeling. Section IV provides some conventional analysis along with the UCRB of the system using only interplane events. Section V expands on the previous section by including detection efficiency criteria by appropriately modeling intraplane and interplane event ratios and weighting them by the intrinsic detection efficiency. Section VI presents results from the M-UCRB study. Appendices A and B provide extra characteristics of the simulated events.

II. CLASSICAL AND BIASED CRAMÉR–RAO LOWER BOUND

The classical CRLB expresses the minimum achievable variance of an unbiased estimator [30], [31]. Let $\underline{\theta} = [\theta_1, \ldots, \theta_j, \ldots, \theta_J]$ express the J-pixel parameterization of the unknown source intensity that is being measured with $\hat{\theta}$ signifying its estimate.[1]

The lower bound of the variance (σ_j^2) of an unbiased estimator $\hat{\theta}_j$ of the jth parameter θ_j has the form

$$\sigma^2\left(\hat{\theta}_j\right) \geq \underline{e}_j^{\mathrm{T}} \mathbf{F}^{-1} \underline{e}_j \tag{1}$$

where $[\ ]^{\mathrm{T}}$ is a transpose operation and $\mathbf{F}$ signifies[2] the fisher information matrix (FIM) further discussed in Section II-A. The unit vector $\underline{e}_j$ is a J-element zero vector with a one in the jth element.

[1]Underlined variables indicate vectors.
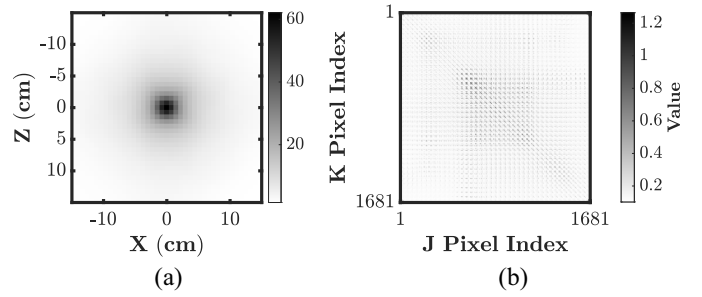[2]Boldfont variables indicate matrices.

Fig. 2. (a) Simple backprojection response of a 718 keV point source for a 12-cm interplane spaced system. (b) Observed FIM. The image space consisted of a 30×30 cm^2 square using 41×41 pixels with $J = 1681$. The $J \times J$ FIM in (b) is challenging to interpret visually because 2-D image space is mapped to 1-D indices along each axis.

A. Fisher Information Matrix

The FIM has the form

$$\mathbf{F} = \mathrm{E}\left\{\left[\nabla_{\underline{\theta}} \ln p\left(\underline{Y}|\underline{\theta}\right)\right]\left[\nabla_{\underline{\theta}} \ln p\left(\underline{Y}|\underline{\theta}\right)\right]^{\mathrm{T}}\right\} \tag{2}$$

where $\underline{Y}$ denotes an observed random variable and $p(\underline{Y}|\theta)$ represents the system matrix as described in [32]. The conditional probability represents the probability of observing $\underline{Y}$ given an event is generated in image bin j. The FIM is, therefore, a matrix of size $J \times J$. It represents a measure of the information the observed $\underline{Y}$ has about the unknown $\underline{\theta}$. When small changes in $\underline{\theta}$ lead to large changes in the measurement distribution, the Fisher information is larger.

An alternative to (2) is the observed FIM [33], [34] with Monte Carlo integration. Its elements are given by

$$\mathrm{F}_{jk}^{\mathrm{obs}} = \frac{\Lambda}{N} \sum_{i=1}^{N} \frac{p(Y_i|j)p(Y_i|k)}{\left(\sum_{q=1}^{J} p(Y_i|q)\theta_q\right)^2} \tag{3}$$

where N is the number of random observations with observation index i and Λ is detection efficiency.

Although other [35] forms of the FIM exist that do not include the Λ/N factor in front, we include it as a means for simplifying the modeling of detection efficiency. Should the factor not be included, the efficiency can be taken into account by N, given that the different observations utilize a source with consistent activity and measurement time characteristics. However, due to the computational expense associated with the simulation and construction of the FIM matrix, we used the same number of observations N across all simulations. To scale the FIM with different efficiencies, we normalized it by dividing by N and scale it with the detection efficiency Λ. Using a large number of observations increases the model accuracy.

Fig. 2(a) shows a simple backprojection image of a simulated point source that is used to compute the observed FIM. Fig. 2(b) shows an example of the FIM.

B. Uniform Cramér–Rao Bound

A limitation of the classical CRLB analysis is that unbiased estimation is often not practical [25]. Regularization is generally applied to reduce noise and variance but reduces spatial
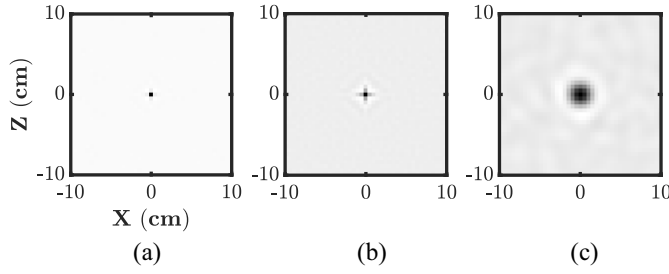
Fig. 3. Mean-gradient ($\nabla_{\underline{\theta}} m$) images of a point source located at the center with different bias norms. This illustrates the effect of bias on $\nabla_{\underline{\theta}} m$ and the square root variance (σ). (a) $\delta = 0.1, \sigma = 8.5$. (b) $\delta = 0.5, \sigma = 2.6$. (c) $\delta = 0.95, \sigma = 0.002$.

resolution (increases bias). Using the UCRB, the limiting variance of an estimator becomes a function of the bias-gradient length [24]. The UCRB, therefore, separates the variance-bias (or sigma-delta) plane into achievable and unachievable regions.

The biased CRLB [36] for the jth element of $\underline{\theta}$ is defined as

$$\sigma^2\left(\hat{\theta}_j\right) \geq \nabla_{\underline{\theta}} m^{\mathrm{T}} \mathbf{F}^{-1} \nabla_{\underline{\theta}} m \qquad (4)$$

where $\nabla_{\underline{\theta}} m = \partial m(\hat{\theta}_j)/\partial \underline{\theta} = \partial \mathrm{E}[\hat{\theta}_j]/\partial \underline{\theta}$ is the mean gradient, i.e., the gradient of the estimator's mean response function ($\mathrm{E}[\hat{\theta}_j]$). Under certain conditions, it can be seen as the point spread function (PSF) and represents the sensitivity of the reconstructed pixel to perturbations in the true parameter. The bias (b), or the difference between the expectation and the true parameter, is defined as

$$b\left(\hat{\theta}_j\right) = \mathrm{E}\left[\hat{\theta}_j\right] - \theta_j. \qquad (5)$$

The J-element bias-gradient vector associated with the jth image pixel is therefore

$$\nabla_{\underline{\theta}} b\left(\hat{\theta}_j\right) = \left[\partial b\left(\hat{\theta}_j\right)/\partial \theta_1, \ldots, \partial b\left(\hat{\theta}_j\right)/\partial \theta_J\right]^{\mathrm{T}}$$
$$= \nabla_{\underline{\theta}} m - \underline{e}_j. \qquad (6)$$

The bias-gradient norm or length of the bias gradient is

$$\delta = \left\|\nabla b_{\underline{\theta}}\right\| = \nabla b\left(\hat{\theta}_j\right)^{\mathrm{T}} \mathbf{I} \nabla b\left(\hat{\theta}_j\right) \qquad (7)$$

where $\mathbf{I}$ is an identity matrix since this work was projected in Euclidean space. Equation (7) also presents a definition of the Euclidean norm. As outlined in [24], under a bias-gradient norm constraint, the limiting variance for a given bias-gradient length is

$$\mathrm{Var}_j^{\mathrm{UCRB}}\left(\hat{\theta}_j, \delta\right) = \sigma^2\left(\hat{\theta}_j, \lambda\right)$$
$$\geq \underline{e}_j^{\mathrm{T}}[\mathbf{I} + \lambda \mathbf{F}]^{-1} \mathbf{F}[\mathbf{I} + \lambda \mathbf{F}]^{-1} \underline{e}_j \qquad (8)$$

with bias-norm

$$\delta = \left\|[\mathbf{I} + \lambda \mathbf{F}]^{-1} \underline{e}_j\right\|. \qquad (9)$$

In (8) and (9), λ represents a Lagrange multiplier as they were derived from a Lagrangian. The $\sigma - \delta$ curve can be traced by sweeping through different values of λ.

Fig. 3 plots several mean gradients [$\nabla_{\underline{\theta}} m$ in (6)] for different bias-gradient lengths, showing the effects of increased bias (smoothing) and the decrease in variance.

C. Modified Uniform Cramér–Rao Bound

There have been some counter-intuitive results originating from the UCRB analysis as different PSFs can have identical bias-gradient norms, but with different resolutions [37]. To overcome this issue, the modified-UCRB (M-UCRB) [38] was developed to study bias-variance tradeoffs by using a resolution constraint. Rather than imposing a constraint on the bias gradient, as done in the UCRB, the M-UCRB solves for the minimum variance for a given distance between the mean gradient and a target/desired mean gradient (f)

$$\left\|\nabla_{\underline{\theta}} m - f\right\| \leq \delta. \qquad (10)$$

The optimum (opt) mean gradient that minimizes the achievable variance under the constraint is given by

$$\nabla_{\underline{\theta}} m^{\mathrm{opt}} = \mathbf{F}[\mathbf{F} + \lambda \mathbf{I}]^{-1} f \qquad (11)$$

with

$$\delta = \left\|[\mathbf{I} + \lambda \mathbf{F}]^{-1} f\right\|. \qquad (12)$$

The minimum achievable variance is then calculated by inserting (11) into (4)

$$\mathrm{Var}_j^{\mathrm{M-UCRB}}\left(\hat{\theta}_j, \delta\right) = \sigma^2\left(\hat{\theta}_j, \lambda\right)$$
$$\geq f^{\mathrm{T}}[\mathbf{F} + \lambda \mathbf{I}]^{-1} \mathbf{F}[\mathbf{F} + \lambda \mathbf{I}]^{-1} f. \qquad (13)$$

The M-UCRB, therefore, allows one to quantify variance based on a maximum allowed distance between the mean gradient and the desired mean gradient. Its use has presented reasonable predictions in comparing different imager designs [39]. It also presents an opportunity to apply the minimum variance tool in scenarios with more exotic sources rather than a point source. Section VI uses the true distribution ($\underline{\theta}$) as the desired target function (f) and models it after a prompt gamma-ray distribution from a certain proton beam. Note that when $f = \underline{e}_j$, the mean-gradient constraint (10) turns into the original UCRB bias-gradient constraint, and (13) reduces to (8). Although not utilized in this study, a vectorized version of the M-UCRB is available in [40], which considered multiple pixels.

III. Simulation Methods

A. CdZnTe Gamma-Ray Imager

This study considers a two plane design with a 3×3 array of crystals in each plane, similar to a previous detector prototype known as Polaris II [41]. The spacing between each crystal is 2.25-cm center-to-center from the neighboring crystal. The crystal's face is 2×2 cm^2 with a thickness of 1.5 cm. The cathode is a planar electrode, while the anode has an 11×11 pixelated array and a pixel pitch of 1.72 mm. This configuration allows for the 3-D reconstruction of each gamma-ray interaction. Fig. 1 sketches the system labeling the front and rear plane whose cathodes both face the $\overrightarrow{y}$-direction. It also depicts a gamma ray emitted from a source that Compton scattered in the front plane and then absorbed in the rear plane. We will refer to it as an "interplane" event, while an "intraplane" event will only interact in a single plane.
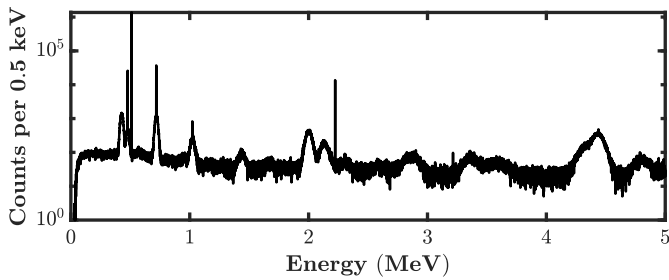
Fig. 4. Simulated gamma-ray spectra of prompt gamma rays emitted from a 100-MeV proton beam incident on HDPE.
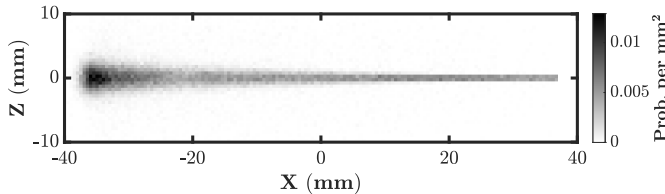

Fig. 5. Simulated distribution sample of origin locations of 4.4-MeV prompt gamma rays from a 100-MeV proton beam incident on HDPE in the $-x$ direction.

We use Geant 4.10.04.p02 [42] to model the response of the CdZnTe imager using the "emstandard" physics constructor. Details regarding the validity simulation, when compared to experiment, are available in [43]. The simulation models the system's configuration of the anode pixels, but gamma-ray pair-production events and timing of gamma-ray interaction were not. Therefore, the response lacks chance-coincidence events but will concatenate multiple interactions for each incident gamma ray if they occur under a single anode pixel into a single event and gives their center of mass as the depth of interaction. In addition, the simulation models the triggering of multiple pixels should the resulting electron traverse across adjacent pixels. The subpixel position estimation capability of the detector was not taken into consideration [44].

B. Simulation of the Gamma-Ray Source

We consider only two gamma-ray source geometries: 1) an isotropic point source and 2) the prompt gammas expected from proton irradiation. All isotropic point source simulations model the source 30 cm away from the front plane's cathode in its isocenter ($\overrightarrow{y}$) using either 718-keV or 4.4-MeV gammas. Even though the energies of the "4.4" peak are 4.438-MeV gamma produced from the $^{12}\mathrm{C}(p, p'\gamma_{4.438})$ $^{12}\mathrm{C}$ reaction and 4.444 MeV from the $^{12}\mathrm{C}(p, 2p\gamma_{4.444})$ $^{11}\mathrm{B}^*$ reaction [29], we assume a single monoenergetic 4.4-MeV source for simplicity.

The physics lists and beam simulation setup utilized to develop the prompt gamma-ray distribution produced from the proton beam are available in [45]. This study shoots a 100-MeV proton beam into a high-density polyethylene (HDPE) target in the $\overrightarrow{x}$ direction. Fig. 4 plots the spectra emitted in that process. We then inject the origin distribution of the prompt gammas into the CdZnTe simulation package. The simulation of the prompt gammas and the Compton camera was applied at different times to reduce computational costs. Therefore, the modeling of the Compton camera's performance did not include the target phantom. Fig. 5 depicts a sample of
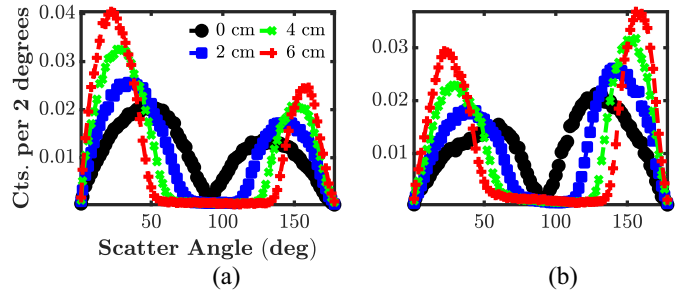

Fig. 6. True recorded scatter angle distribution for (a) 718-keV and (b) 4.4-MeV source for two-interaction interplane events only.

the 4.4-MeV prompt gamma-ray origins with its perigee 30 cm away from the front plane's cathode surface.

C. Imaging and Processing of Simulation

Different interplane spacings were simulated that ranged from 0 to 20 cm in steps of 2 cm. The UMImaging image reconstruction package [46] was used to create the system response vectors. To do so, it projected Compton events comprised of only 2, 3, 4, and 5 pixel events on a 30×30 cm^2 Cartesian image space with a 41×41 pixel grid. Each system response vector, $p(Y_i|j)$ from (3), accounted for the Klein–Nishina cross section of each scatter, attenuation probabilities, and photoelectric cross section for the absorbed interaction. In addition, the position resolution was modeled as described in [47] and [48].The interactions within a single event cannot be sequenced temporally as the timing resolution of CdZnTe is poor relative to the time interval between interactions. Therefore, the system response considers all sequence permutations. Side-neighboring events, or events in which two adjacent pixels were triggered, were ignored.

IV. BIAS-VARIANCE TRADE-OFF ANALYSIS OF ONLY INTERPLANE EVENTS

This section presents results from the CRLB analysis from a point source and considers the two energies. The $\sigma - \delta$ curves present the results and outline the minimum achievable variance response for a given bias length. Each σ is calculated as the square root of the variance, $\sigma = \sqrt{\mathrm{Var}}$. Naturally, we desire a smaller variance for the given bias-norm. This section does not consider detector efficiency and therefore, uses a $\Lambda = 1$ when constructing the FIM. Throughout this work, the chosen pixel for which $e_j = 1$ is such that the jth pixel is in the center of the image space, $(X, Z) = (0, 0)$.

A. Traditional Analysis of Interplanar Events

Fig. 6 plots the distribution of the true recorded scatter angles for two-pixel events from: 1) 718-keV or 2) 4.4-MeV gamma rays, which were fully absorbed in the detector. As expected, the distribution is bimodal with smaller scatter angles signifying a scatter off the front plane and absorption in the rear, while larger angle scatters signify a scatter off the rear plane and absorption in the front. It shows that increasing the interplane spacing polarizes the distribution to either the 0° or 180° extremes. However, when comparing the distribution
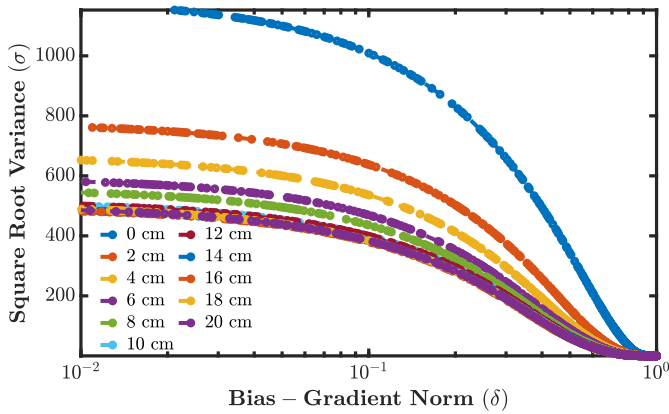
Fig. 7. Sigma-delta curves for different detector spacings and their response to the 718-keV point source using only interplanar events. The upper right section of the graph presents an achievable region, while the lower left would be an unachievable one.
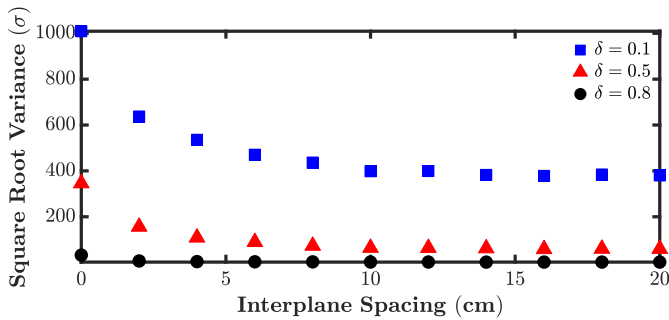

Fig. 8. Sigma-interplane spacing response for different biases for a 718-keV point source.

between the two energies, back scatters are favored for the 4.4-MeV distribution, while forward scatters are favored for the 718-keV distribution when only considering fully absorbed events. Appendix A provides a similar analysis for three-or-more interaction events as the distribution significantly differs from two-interaction events.

B. UCRB Analysis of Interplanar Events

Fig. 7 plots the $\sigma - \delta$, or the square root of the estimator's variance of $\hat{\theta}_j$ versus the bias-gradient norm, curves for the different systems when using a 718-keV point source placed in the center of the image space. As these are difficult to interpret and therefore not informative, the $\sigma - \delta$ response is only analyzed for three bias-gradient lengths ($\delta = 0.1, 0.5, 0.8$). Fig. 8 plots the σ-interplane spacing curves and shows the responses plateauing at around 12 cm for all biases indicating that larger spacings result in minimal returns in imaging performance.

Fig. 9 plots the σ-interplane spacing response for a 4.4-MeV point source. Like its 718-keV counterpart, it also plateaus, but at a smaller interplane distance of 6 cm. This demonstrates the different responses of the imager to the different energies.

V. UCRB ANALYSIS WITH DETECTION EFFICIENCY

The analysis in Section IV only used interplane events and did not include any detection efficiency criteria. As the interplane spacing increases, the system will experience a
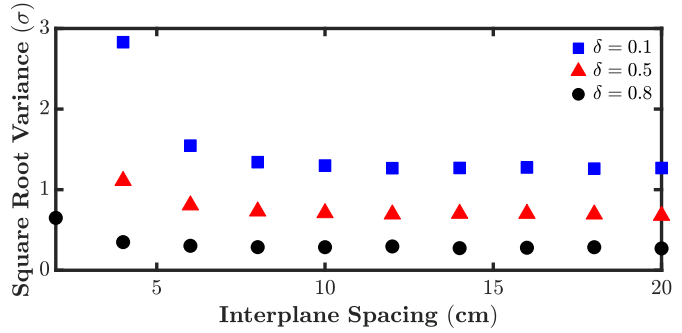

Fig. 9. Sigma-interplane spacing response for different biases for a 4.4-MeV point source. The scale was trimmed to $0 \leq \sigma \leq 3$.
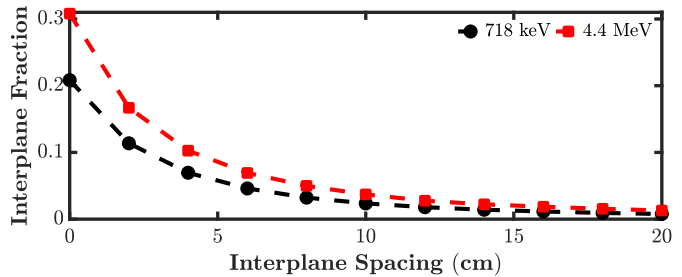

Fig. 10. Fraction of interplane events to total events for simulated responses to 718-keV and 4.4-MeV point sources.

loss in detection efficiency, especially with interplane events. Therefore, a new FIM was constructed that uses all events, intraplane and interplane. Next, we account for the intrinsic detection efficiency of the system by using the weighting factor Λ as an efficiency criterion that scales the FIM. Therefore, this section will present a more practical analysis as proton therapy and other applications may be count-rate-limited scenarios.

A. Intraplane and Interplane Events Analysis

A new FIM was constructed with a simulation that models both intraplane and interplane events. Naturally, as the interplane spacing increases, single-plane events will dominate the event distribution. Fig. 10 demonstrates this effect by plotting the fraction between interplane and all events, showing a near inverse-squared relationship with the interplane distance. That behavior also indicates that in a count-rate-limited application, strictly using interplane events may not be practical. Appendix B provides an analysis of the recorded scatter angle for intraplane and interplane events.

Fig. 11 plots the new σ values for different interplane spacing designs for certain biases. In this representation, the σ values were normalized by the standard deviation of the designs with zero interplane spacings for the given bias: $\sigma(interplane\ spacing, \delta)/\sigma(0, \delta)$. This normalization was applied to highlight the general trend rather than present specific values. Note that Λ in this section is still 1. Comparing Fig. 11 with Fig. 9, which does not include intraplane events, a noticeable change in trend is observed. Rather than plateauing, the performance degrades for larger interplane spacing. That was expected as the interplane efficiency between the two planes becomes negligible for very large spacings. The
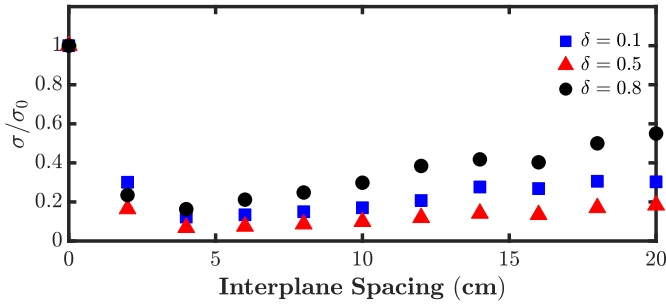
Fig. 11. Sigma-delta curves for different detector spacing and their response to the 4.4-MeV point source for both interplane and intraplane events. The trend shows a minimum of around 4 cm. The σ values were normalized by the standard deviation of the designs with zero interplane spacings (σ_0).
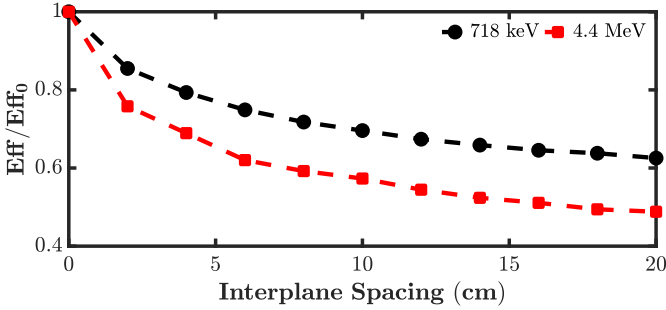

Fig. 12. Detection efficiency normalized to the 0 cm plane separation case. It was calculated from a point source located 30 cm away from the face of the detector along the $\hat{y}$ axis.
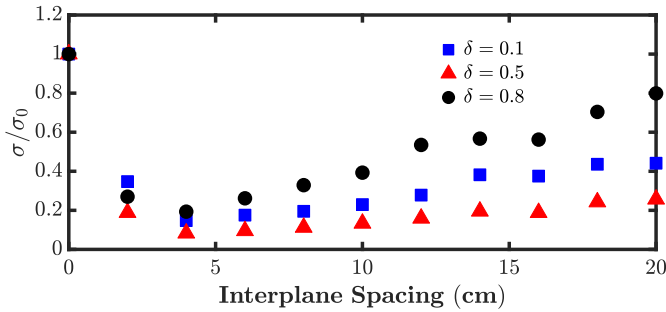

Fig. 13. Sigma-delta curves for different detector spacings and their response to the 4.4-MeV point source when considering both intraplane and interplane events with efficiency scaling. The σ values were normalized by the standard deviation of the designs with zero interplane spacings (σ_0).

minimum at 4 cm indicates the optimized detector design for the given criteria.

B. Accounting for Intrinsic Efficiency

In addition to the change of intraplane and interplane efficiencies, the overall intrinsic efficiency also changes with interplane spacing. Fig. 12 plots the detection efficiency normalized to the zero detector spacing case. The efficiency is then factored into the FIM with Λ in (3).

Fig. 13 plots the new σs with the added efficiency criteria and again normalized to the σ of the zero spaced detectors. When comparing the plot with Fig. 11, the normalized standard deviation increases relative to the values that did not consider efficiency. That was expected as the poorer efficiency for the larger spaced detectors results in increased variance.
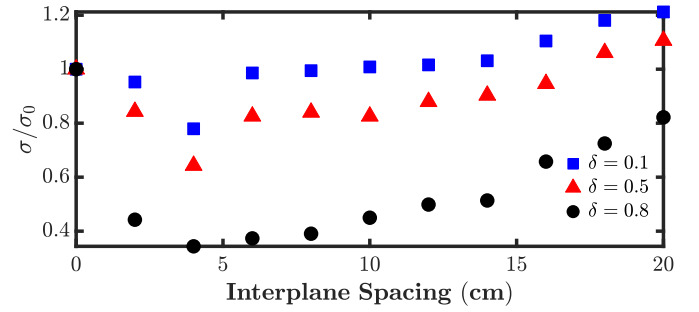

Fig. 14. Sigma-delta curves for different detector spacings and their response to the 718-keV point source when considering both intraplane and interplane events with efficiency scaling. The σ values were normalized by the standard deviation of the designs with zero interplane spacings (σ_0).
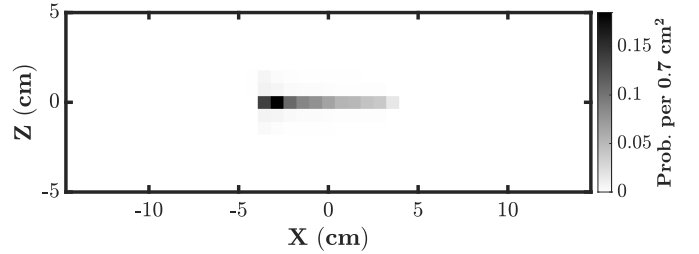

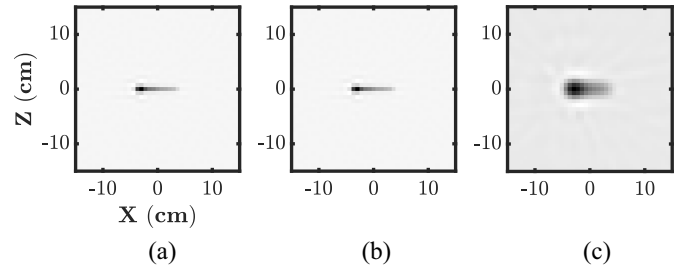Fig. 15. Target function f projected onto the image space.

Fig. 16. Mean-gradient ($\nabla_{\underline{\theta}} \underline{m}^{\mathrm{opt}}$) images with different bias-gradient norms to illustrate the effect of increased bias on it as used in the modified UCRB. The plots present different bias-gradient norms of (a) $\delta = 0.1$, (b) $\delta = 0.15$, and (c) $\delta = 0.25$.

The figure also indicates that the optimized detector spacing for imaging a 4.4-MeV point source located 30 cm away from the detector is about 4 cm when using intraplane and interplane events with efficiency considerations. Fig. 14 plots the 718-keV counterpart with a similar trend.

VI. Modified Uniform Cramér–Rao Bound Results

As discussed in Section II, the M-UCRB uses a mean-gradient constraint rather than a bias-gradient constraint to calculate the lower variance. That also allows for the analysis of detector designs and their response to a prompt gamma-ray distribution from proton irradiation. Fig. 15 plots the target function, f from (13). Fig. 16 gives an idea of the mean gradient with different bias-gradient norms.

Next, using M-UCRB, we analyze different interplane spacings by varying the mean gradient with the Lagrange multiplier which results in Fig. 17. The analysis includes both intraplane and interplane events and considers the change of detection efficiency as done in Section V-B. Unlike the UCRB, which
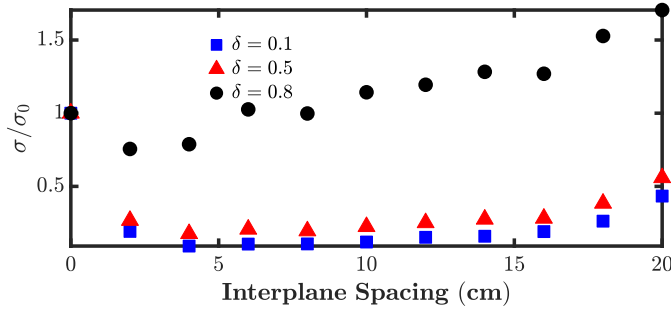
Fig. 17. Sigma-delta curves for different detector spacings using the M-UCRB analysis. The plot shows the minimum variance response to a target function modeled after the prompt gamma-ray distribution one would expect from proton irradiation on HDPE. The vertical axis represents σ values that were normalized by the standard deviation of the designs with zero interplane spacings (σ_0).

has a bias-gradient norm ranging from 0 to 1, the σs quickly reduce to near zero at $\delta > 0.3$. Therefore, the plot only considers bias-gradient norms of $\delta = 0.05, 0.15, 0.25$. Once again, the σ values are normalized to the 0 cm interplane spacing to highlight the general trend. Unlike the previous tradeoff plots, the ideal design for the given δ is different for the low and high bias cases. The low bias cases have a low concavity near the minimum, which is at 4 cm. On the other hand, the high bias cases have a more defined minimum of around 2 cm.

VII. DISCUSSION

This work shows the effects of interplane spacing design and the effects of different event selections on the achievable minimum variance. When considering only interplane events, without any detection efficiencies, the performance plateaus after a certain distance. However, the performance of larger spacing degrades when considering both intraplane and interplane events with detection efficiency. Moreover, these considerations indicate an optimized spacing of around 4 cm for the studied geometries.

The M-UCRB analysis also gives similar results. However, the optimized spacing differs when considering different bias-gradient norms. The results suggest an interplane spacing of around 4 cm in lower biases but closer to 2 cm at higher biases. To choose the appropriate spacing, one must consider the desired resolution and match that with the predicted mean-gradient response ($\nabla_{\underline{\theta}} m^{\text{opt}}$) (the PSF).

A. UCRB Analysis Limitations

The optimization of the interplane spacing is valid only for the considered scenarios. A different number of crystals and sizes could alter the results. Also, varying the image space might change the response. The analysis also does not account for artifacts that occur outside the image field of view. These artifacts could be from missequenced rings or contamination from other detector effects, such as chance coincidence or pair production [49]. However, the limited field of view is acceptable in the range verification application as the prompt gammas of interest originate from a specific region. Finally, this analysis is limited to 2-D source distribution estimation. The study should be expanded to three dimensions as the end goal is 3-D dose estimation.

B. Modeling Deficits

There are several effects not considered when modeling the detector response. First, the simulation did not model chance coincidence events and did not include pair-production physics. Although they can affect the results, modern techniques are being developed that can discriminate against them [50] and [51]. The simulation also does not model energy threshold or other detector effects, such as charge leakage, efficiency losses due to the guard ring, and poor anode side reconstruction. Such effects reduce the detector's efficiency and we, therefore, underestimate the system's variance [43].

Next, the simulation of the point and prompt gamma source does not consider any environmental effects, such as room return or the patient's anatomy. Such effects add background and noise to the image. In addition, no secondary particles or gamma rays from neutron productions are considered [52].

Finally, the system response model was based on Wilderman *et al.* [32]. Any model mismatch will bias the results.

VIII. CONCLUSION AND FUTURE WORK

We presented a method to optimize a Compton imager's performance with the UCRB and its modified variation for imaging prompt gamma rays from proton irradiation. It is perhaps more informative than simple analytical models, as shown in [53], as they may not present the intrinsic image resolution.

This work studied the bias-variance response of an 18 crystal system arranged into two 3×3 arrays and investigated the response for different interplane separations using the 718-keV and 4.4-MeV prompt gammas. The optimization of the interplane distance is of great interest because of its effects on the recorded distance between the first and second interaction. As outlined in [54], the contribution of the interaction's positional uncertainty to the image resolution is related to that distance. The interplane spacing also alters the distribution of recorded scatter angles and affects the image resolution as shown in [55].

Using only interplanar events, the critical point for the variance-plane separation curve for both energies occurs at different distances. The critical point, or where the derivative is near zero, occurs at 10 cm for the 718-keV case as opposed to 8 cm for 4.4-MeV. When considering all event types, the performance of imagers with larger interplanar spacing severely degrades. Moreover, Figs. 13 and 14 present a clear minimum of around 4 cm. The performance of larger spacings further deteriorates when considering the detection efficiency.

Finally, the M-UCRB was utilized to investigate how a more realistic source might affect the design. Unlike the UCRB results, the optimized interplane spacing was different for low and high bias-norm cases. For low bias, the optimized design is around 4 cm while the high bias cases have a defined minimum at around 2 cm.

This study was limited to the current available CdZnTe detector technology. However, new systems are currently under investigation that use larger CdZnTe crystals [56] or techniques that allow for more flexible detector geometries. More
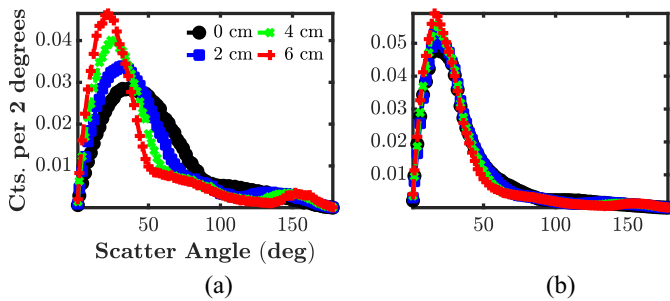
Fig. 18. Recorded scatter angle distribution for 3-or-more interactions from (a) 718-keV and (b) 4.4-MeV source. Note that only interplane events were utilized.
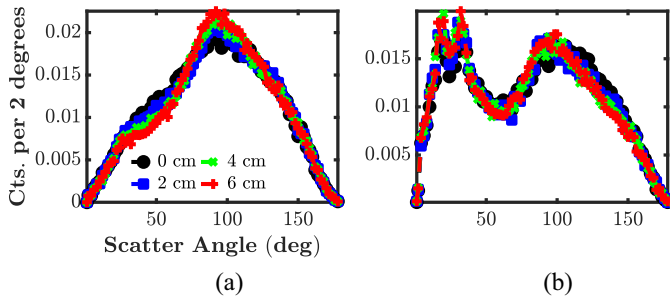

Fig. 19. Recorded scatter angle distribution for (a) 718-keV and (b) 4.4-MeV source for two-interaction using intraplane and interplane events.

modular systems can allow for more complex designs and should expand the design criteria accordingly.

Beam range verification can also be accomplished via spectroscopic or aperture-based imagers and should be compared to Compton imaging using this technique. Such an analysis would be useful as it would inform on the best techniques for the application. Since range verification can use multiple observables, such as energy spectra, timing, and even acoustical signatures [57], those signals should be factored into the FIM.

APPENDIX A
SCATTER DISTRIBUTION FOR 3-OR-MORE PIXEL EVENTS

Fig. 18 plots the distribution of scatter angles recorded for interplane events that triggered 3-or-more pixels. Unlike the two pixel events, which have a bimodal distribution, the plot appears to be skewed right. Comparing Fig. 18(a) and (b), the hint of the backscatter peak vanishes. This is because backscattered gamma rays asymptotically reach $E_0/(1 + 2E_0/m_0c^2) \approx 256$ keV when the incident energies are large ($E_0 \gg m_0c^2/2$) [3]. It is around 250 keV where the photoelectric absorption and the Compton scattering cross sections intersect for CdZnTe. Therefore, events that backscatter will most likely result in two interaction events for the given geometry.

APPENDIX B
SCATTER DISTRIBUTION FOR INTRA- AND INTER-PLANAR EVENTS

To contrast the distribution that Fig. 6 plots, Fig. 19 plots the distribution for two interaction events for both 718-keV

and 4.4-MeV gammas considering intraplane and interplanar events. In the plot, 90° scatter angles dominate the distributions as they are mainly intraplane events.

REFERENCES

[1] *Particle Therapy Co-Operative Group*. Accessed: May 29, 2021. [Online]. Available: https://www.ptcog.ch/
[2] R. R. Wilson, "Radiological use of fast protons," *Radiology*, vol. 47, no. 5, pp. 487–491, 1946. [Online]. Available: https://doi.org/10.1148/47.5.487
[3] G. Knoll, *Radiation Detection and Measurement*. New York, NY, USA: Wiley, 2000.
[4] W. U. Shipley *et al.*, "Advanced prostate cancer: The results of a randomized comparative trial of high dose irradiation boosting with conformal protons compared with conventional dose irradiation using photons alone," *Int. J. Radiat. Oncol. Biol. Phys.*, vol. 32, no. 1, pp. 3–12, 1995. [Online]. Available: http://www.sciencedirect.com/science/article/pii/0360301695000635
[5] V. Patera and A. Sarti, "Recent advances in detector technologies for particle therapy beam monitoring and dosimetry," *IEEE Trans. Radiat. Plasma Med. Sci.*, vol. 4, no. 2, pp. 133–146, Mar. 2020.
[6] K. Parodi and J. C. Polf, "In vivo range verification in particle therapy," *Med. Phys.*, vol. 45, no. 11, pp. e1036–e1050, 2018. [Online]. Available: https://aapm.onlinelibrary.wiley.com/doi/abs/10.1002/mp.12960
[7] G. W. Bennett, J. O. Archambeau, B. E. Archambeau, J. I. Meltzer, and C. L. Wingate, "Visualization and transport of positron emission from proton activation in vivo," *Science*, vol. 200, no. 4346, pp. 1151–1153, 1978. [Online]. Available: https://science.sciencemag.org/content/200/4346/1151
[8] J. M. Verburg and J. Seco, "Proton range verification through prompt gamma-ray spectroscopy," *Phys. Med. Biol.*, vol. 59, no. 23, pp. 7089–7106, Nov. 2014. [Online]. Available: https://doi.org/10.108%2F0031-915%2F5%2F2%2F7089
[9] C. Golnik *et al.*, "Range assessment in particle therapy based on prompt γ-ray timing measurements," *Phys. Med. Biol.*, vol. 59, no. 18, pp. 5399–5422, Aug. 2014. [Online]. Available: https://doi.org/10.1088/0031-9155/59/18/5399
[10] J. Krimmer *et al.*, "A cost-effective monitoring technique in particle therapy via uncollimated prompt gamma peak integration," *Appl. Phys. Lett.*, vol. 110, no. 15, 2017, Art. no. 154102. [Online]. Available: https://doi.org/10.1063/1.4980103
[11] M. Fontana *et al.*, "Monitoring ion beam therapy with a compton camera: Simulation studies of the clinical feasibility," *IEEE Trans. Radiat. Plasma Med. Sci.*, vol. 4, no. 2, pp. 218–232, Mar. 2020.
[12] F. Hueso-González *et al.*, "Compton camera and prompt gamma ray timing: Two methods for in vivo range assessment in proton therapy," *Front. Oncol.*, vol. 6, p. 80, Apr. 2016. [Online]. Available: https://www.frontiersin.org/article/10.3389/fonc.2016.00080
[13] J. Ellin *et al.*, "Evaluation of a novel multi-slit collimated detection system for prompt gamma-ray imaging during proton beam therapy," in *Proc. IEEE Nucl. Sci. Symp. Med. Imag. Conf. (NSS/MIC)*, Sydney, NSW, Australia, 2018, pp. 1–8.
[14] C. Richter *et al.*, "First clinical application of a prompt gamma based in vivo proton range verification system," *Radiother. Oncol.*, vol. 118, no. 2, pp. 232–237, 2016. [Online]. Available: http://www.sciencedirect.com/science/article/pii/S0167814016000074
[15] R. W. Todd, J. M. Nightingale, and D. B. Everett, "A proposed γ camera," *Nature*, vol. 251, no. 5471, pp. 132–134, 1974.
[16] J. C. Polf, S. Avery, D. S. Mackin, and S. Beddar, "Imaging of prompt gamma rays emitted during delivery of clinical proton beams with a compton camera: Feasibility studies for range verification," *Phys. Med. Biol.*, vol. 60, no. 18, pp. 7085–7099, Aug. 2015. [Online]. Available: https://doi.org/10.108%2F0031-915%2F6%2F1%2F7085

[17] S. Mochizuki *et al.*, "High-precision compton imaging of 4.4 MeV prompt gamma-ray toward an on-line monitor for proton therapy," *Nucl. Instrum. Methods Phys. Res. A, Accelerators Spectrometers Detectors Assoc. Equip.*, vol. 936, pp. 43–45, Aug. 2019.

[18] P. Solevi *et al.*, "Performance of MACACO compton telescope for ion-beam therapy monitoring: First test with proton beams," *Phys. Med. Biol.*, vol. 61, no. 14, pp. 5149–5165, Jun. 2016. [Online]. Available: https://doi.org/10.108%2F0031-915%2F6%2F1%2F5149

[19] M.-H. Richard *et al.*, "Design guidelines for a double scattering compton camera for prompt-γ imaging during ion beam therapy: A Monte Carlo simulation study," *IEEE Trans. Nucl. Sci.*, vol. 58, no. 1, pp. 87–94, Feb. 2011.

[20] P. G. Ortega *et al.*, "Noise evaluation of compton camera imaging for proton therapy," *Phys. Med. Biol.*, vol. 60, no. 5, pp. 1845–1863, Feb. 2015. [Online]. Available: https://doi.org/10.108%2F0031-915%2F6%2F5%2F1845

[21] J. C. Polf, D. Mackin, E. Lee, S. Avery, and S. Beddar, "Detecting prompt gamma emission during proton therapy: The effects of detector size and distance from the patient," *Phys. Med. Biol.*, vol. 59, no. 9, pp. 2325–2340, Apr. 2014. [Online]. Available: https://doi.org/10.108%2F0031-915%2F5%2F9%2F2325

[22] S. W. Peterson, D. Robertson, and J. Polf, "Optimizing a three-stage compton camera for measuring prompt gamma rays emitted during proton radiotherapy," *Phys. Med. Biol.*, vol. 55, no. 22, pp. 6841–6856, Nov. 2010. [Online]. Available: https://doi.org/10.108%2F0031-915%2F5%2F2%2F015

[23] H. H. Chen-Mayer, S. Brown, and H. Yang, "Feasibility study of compton imaging for PGAA," *J. Radioanal. Nucl. Chem.*, vol. 322, no. 3, pp. 1729–1738, 2019. [Online]. Available: https://doi.org/10.1007/s10967-019-06818-w

[24] A. O. Hero, J. A. Fessler, and M. Usman, "Exploring estimator bias-variance tradeoffs using the uniform CR bound," *IEEE Trans. Signal Process.*, vol. 44, no. 8, pp. 2026–2041, Aug. 1996.

[25] N. H. Clinthorne *et al.*, "Determining detector requirements for medical imaging applications," *Nucl. Instrum. Methods Phys. Res. A, Accelerators Spectrometers Detectors Assoc. Equip.*, vol. 409, nos. 1–3, pp. 501–507, 1998.

[26] C. H. Hua, N. H. Clinthorne, S. J. Wilderman, J. W. LeBlanc, and W. L. Rogers, "Quantitative evaluation of information loss for compton cameras," *IEEE Trans. Nucl. Sci.*, vol. 46, no. 3, pp. 587–593, Jun. 1999.

[27] L. Han, W. L. Rogers, S. S. Huh, and N. Clinthorne, "Statistical performance evaluation and comparison of a compton medical imaging system and a collimated anger camera for higher energy photon imaging," *Phys. Med. Biol.*, vol. 53, no. 24, pp. 7029–7045, 2008.

[28] E. Lens, E. Tolboom, and D. R. Schaart, "An approach for optimizing prompt gamma photon-based range estimation in proton therapy using Cramér-Rao theory," *IEEE Trans. Radiat. Plasma Med. Sci.*, vol. 4, no. 2, pp. 161–169, Mar. 2020.

[29] B. Kozlovsky, R. J. Murphy, and R. Ramaty, "Nuclear deexcitation gamma-ray lines from accelerated particle interactions," *Astrophys. J. Suppl. Series*, vol. 141, no. 2, pp. 523–541, 2002. [Online]. Available: https://doi.org/10.108%2F340545

[30] C. Rao and S. D. Gupta, *Selected Papers of C.R. Rao*, vol. 4. Calcutta, India: Indian Stat. Inst., 1989. [Online]. Available: https://books.google.com/books?id=m6wRetZkaYAC

[31] H. Cramér, *Mathematical Methods of Statistics (PMS-9), Volume 9*. Princeton, NJ, USA: Princeton Univ. Press, Jun. 2016. [Online]. Available: https://www.degruyter.com/princetonup/view/title/524978

[32] S. J. Wilderman, N. H. Clinthorne, J. A. Fessler, and W. L. Rogers, "List-mode maximum likelihood reconstruction of compton scatter camera images in nuclear medicine," in *Proc. IEEE Nucl. Sci. Symp. Conf. Rec. IEEE Nucl. Sci. Symp. Med. Imag. Conf.*, vol. 3. Toronto, ON, Canada, 1998, pp. 1716–1720.

[33] L. J. Meng and D. K. Wehe, "Feasibility study of using hybrid collimation for nuclear environmental imaging," *IEEE Trans. Nucl. Sci.*, vol. 50, no. 4, pp. 1103–1110, Aug. 2003.

[34] J. O. Berger, *Statistical Decision Theory and Bayesian Analysis* (Springer Series in Statistics). New York, NY, USA: Springer, 1985. [Online]. Available: https://www.springer.com/gp/book/9780387960982

[35] L. Parra and H. H. Barrett, "List-mode likelihood: Em algorithm and image quality estimation demonstrated on 2-D pet," *IEEE Trans. Med. Imag.*, vol. 17, no. 2, pp. 228–235, Apr. 1998.

[36] H. Van Trees, *Detection, Estimation, and Modulation Theory, Part II: Nonlinear Modulation Theory*. New York, NY, USA: Wiley, 2001.

[37] T. J. Kragh and A. O. Hero, "Bias-resolution-variance tradeoffs for single pixel estimation tasks using the uniform Cramér-Rao bound," in *Proc. IEEE Nucl. Sci. Symp. Conf. Rec.*, vol. 2, 2000, pp. 15296–15298.

[38] L. J. Meng and N. H. Clinthorne, "A modified uniform Cramer-Rao bound for multiple pinhole aperture design," *IEEE Trans. Med. Imag.*, vol. 23, no. 7, pp. 896–902, Jul. 2004.

[39] L. J. Meng, N. H. Clinthorne, S. Skinner, R. V. Hay, and M. Gross, "Design and feasibility study of a single photon emission microscope system for small animal I-125 imaging," *IEEE Trans. Nucl. Sci.*, vol. 53, no. 3, pp. 1168–1178, Jun. 2006.

[40] L.-J. Meng and N. Li, "A vector uniform Cramer-Rao bound for SPECT system design," *IEEE Trans. Nucl. Sci.*, vol. 56, no. 1, pp. 81–90, Feb. 2009.

[41] Y. A. Boucher, "Analysis of cadmium zinc telluride detector performance and characteristics for applications in gamma-ray imaging spectrometers," Ph.D. dissertation, Dept. Nucl. Eng. Radiol. Sci., Univ. Michigan, Ann Arbor, MI, USA, 2013. [Online]. Available: http://hdl.handle.net/2027.42/98075

[42] J. Allison *et al.*, "Recent developments in geant4," *Nucl. Instrum. Methods Phys. Res. A, Accelerators Spectrometers Detectors Assoc. Equip.*, vol. 835, pp. 186–225, Nov. 2016. [Online]. Available: http://www.sciencedirect.com/science/article/pii/S0168900216306957

[43] Z. Chen, Y. Zhu, and Z. He, "Intrinsic photopeak efficiency measurement and simulation for pixelated CdZnTe detector," *Nucl. Instrum. Methods Phys. Res. A, Accelerators Spectrometers Detectors Assoc. Equip.*, vol. 980, Nov. 2020, Art. no. 164501. [Online]. Available: http://www.sciencedirect.com/science/article/pii/S0168900220308986

[44] Y. Zhu, S. E. Anderson, and Z. He, "Sub-pixel position sensing for pixelated, 3-D position sensitive, wide band-gap, semiconductor, gamma-ray detectors," *IEEE Trans. Nucl. Sci.*, vol. 58, no. 3, pp. 1400–1409, Jun. 2011.

[45] P. Maggi *et al.*, "Computational model for detector timing effects in compton-camera based prompt-gamma imaging for proton radiotherapy," *Phys. Med. Biol.*, vol. 65, no. 12, Jun. 2020, Art. no. 125004. [Online]. Available: https://doi.org/10.108%2F1361-656%2Fab8bf0

[46] C. G. Wahl, J. M. Jaworski, and Z. He, "UMImaging: A software package for image reconstruction from 3D-position-sensitive gamma-ray detectors," *IEEE Trans. Nucl. Sci.*, vol. 59, no. 4, pp. 1672–1680, Aug. 2012.

[47] D. Xu, "Gamma-ray imaging and polarization measurement using 3-D position-sensitive CdZnTe detectors," Ph.D. dissertation, Dept. Nucl. Eng. Radiol. Sci., Univ. Michigan, Ann Arbor, MI, USA, 2006.

[48] W. Wang, C. G. Wahl, J. M. Jaworski, and Z. He, "Maximum-likelihood deconvolution in the spatial and spatial-energy domain for events with any number of interactions," *IEEE Trans. Nucl. Sci.*, vol. 59, no. 2, pp. 469–478, Apr. 2012.

[49] D. Shy, J. Xia, and Z. He, "Artifacts in high-energy compton imaging with 3-D position-sensitive CdZnTe," *IEEE Trans. Nucl. Sci.*, vol. 67, no. 8, pp. 1920–1928, Aug. 2020.

[50] A. Zoglauer, "Using deep learning for the event reconstruction of combined compton-scattering and pair-creation telescopes," in *Proc. Amer. Astron. Soc. Meeting Abstracts #235*, vol. 235, Jan. 2020, Art. no. 372.21.

[51] E. Muñoz *et al.*, "Proton range verification with MACACO II compton camera enhanced by a neural network for event selection," *Sci. Rep.*, vol. 11, no. 1, pp. 1–12, 2021.

[52] R. Panthi, P. Maggi, S. Peterson, D. Mackin, J. Polf, and S. Beddar, "Secondary particle interactions in a compton camera designed for in vivo range verification of proton therapy," *IEEE Trans. Radiat. Plasma Med. Sci.*, vol. 5, no. 3, pp. 383–391, May 2021.

[53] D. W. Mundy and M. G. Herman, "Uncertainty analysis of a compton camera imaging system for radiation therapy dose reconstruction," *Med. Phys.*, vol. 37, no. 5, pp. 2341–2350, 2010. [Online]. Available: https://aapm.onlinelibrary.wiley.com/doi/abs/10.1118/1.3399777

[54] C. E. Ordonez, W. Chang, and A. Bolozdynya, "Angular uncertainties due to geometry and spatial resolution in compton cameras," *IEEE Trans. Nucl. Sci.*, vol. 46, no. 4, pp. 1142–1147, Aug. 1999.

[55] C. E. Ordonez, A. Bolozdynya, and W. Chang, "Dependence of angular uncertainties on the energy resolution of compton cameras," in *Proc. IEEE Nucl. Sci. Symp. Conf. Rec.*, vol. 2. Albuquerque, NM, USA, 1997, pp. 1122–1125.

[56] Y. Zhu and Z. He, "Performance of larger-volume $40 \times 40 \times 10-$ and $40 \times 40 \times 15-$mm^3 CdZnTe detectors," *IEEE Trans. Nucl. Sci.*, vol. 68, no. 2, pp. 250–255, Feb. 2021.

[57] J. C. Polf and K. Parodi, "Imaging particle beams for cancer treatment," *Phys. Today*, vol. 68, no. 10, pp. 28–33, 2015.